A HYBRID MAGNETICALLY/THERMALLY-DRIVEN WIND IN THE BLACK HOLE GRO J1655–40?

Joseph Neilsen[1], Jeroen Homan[1]
Draft version February 29, 2012

ABSTRACT

During its 2005 outburst, GRO J1655–40 was observed twice with the *Chandra* High Energy Transmission Grating Spectrometer; the second observation revealed a spectrum rich with ionized absorption lines from elements ranging from O to Ni (Miller et al. 2006a, 2008; Kallman et al. 2009), indicative of an outflow too dense and too ionized to be driven by radiation or thermal pressure. To date, this spectrum is the only definitive evidence of an ionized wind driven off the accretion disk by magnetic processes in a black hole X-ray binary. Here we present our detailed spectral analysis of the first *Chandra* observation, nearly three weeks earlier, in which the only signature of the wind is the Fe XXVI absorption line. Comparing the broadband X-ray spectra via photoionization models, we argue that the differences in the *Chandra* spectra cannot possibly be explained by the changes in the ionizing spectrum, which implies that the properties of the wind cannot be constant throughout the outburst. We explore physical scenarios for the changes in the wind, which we suggest may begin as a hybrid MHD/thermal wind, but evolves over the course of weeks into two distinct outflows with different properties. We discuss the implications of our results for the links between the state of the accretion flow and the presence of transient disk winds.

Subject headings: accretion, accretion disks — black hole physics — X-rays: individual (GRO J1655–40) — X-rays: binaries — stars: winds, outflows

1. INTRODUCTION

The last two decades have seen the discovery of a multitude of highly-ionized absorbers and winds in the X-ray spectra of accreting black hole and neutron star X-ray binaries (e.g. Ebisawa 1997; Kotani et al. 1997; Brandt & Schulz 2000; Kotani et al. 2000a,b; Lee et al. 2002; Schulz & Brandt 2002; Ueda et al. 2004; Miller et al. 2004, 2006a,b, 2008; Neilsen & Lee 2009; Ueda et al. 2009; Blum et al. 2010; Reynolds & Miller 2010; Miller et al. 2011; Neilsen et al. 2011, 2012; King et al. 2012). In many of these cases, although the kinetic power in these outflows is orders of magnitude below the accretion power, the mass loss rate in the wind can be much greater than the accretion rate at the inner edge of the disk (e.g. Neilsen et al. 2011). The ubiquity of disk winds in X-ray binaries and their extreme mass loss rates suggests that these outflows play a crucial role in the physics of accretion.

Presently, accretion disk winds are understood to be driven by some combination of radiation, thermal, and magnetic pressure, which operate in different regimes of density and ionization (Begelman et al. 1983; Proga 2000; Proga & Kallman 2002; Miller et al. 2006a). Yet determining which of these processes dominates the physics of an individual outflow typically presents a significant challenge. Most often, indirect density estimates must come from geometrical arguments that constrain the distance R of the wind from the black hole (e.g. Lee et al. 2002; Neilsen et al. 2011, 2012). In these cases, the density n can be found using the observed ionization parameter ξ and luminosity L (Tarter et al. 1969):

$$\xi = \frac{L}{nR^2}. \tag{1}$$

[1] MIT Kavli Institute for Astrophysics and Space Research, Cambridge, MA 02139; jneilsen@space.mit.edu

In rare cases it may be possible to measure the density directly from density-sensitive atomic lines, a technique that was most notably applied in the discovery of a magnetically-driven wind in GRO J1655–40 (Miller et al. 2006a, hereafter M06). When *Chandra* observed this microquasar with the High Energy Transmission Grating Spectrometer (HETGS; Canizares et al. 2005) in the middle of its 2005 outburst, the high-resolution X-ray spectrum (ObsID 5461) revealed a rich series of absorption lines from a dense ($n \gtrsim 10^{14}$ cm^{-3}), highly-ionized ($\xi \sim 10^4$) wind. Detailed follow-up spectral analysis and theoretical studies (Miller et al. 2008, hereafter M08; Kallman et al. 2009, hereafter K09; Luketic et al. 2010) have repeatedly confirmed the original conclusion of M06: this outflow was driven primarily via magnetic processes, rather than radiation or thermal pressure.

However, a HETGS observation (ObsID 5460) of the same outburst made 20 days earlier reveals an outflow that is empirically quite different (see Figure 1). Instead of the host of lines, this observation merely contains an Fe XXVI absorption line noted in passing by M08. In this paper, we ask: where did the other lines go? During the first observation, are we simply observing a much more ionized (and thus transparent) version of the wind studied by M06, M08, and K09? Or do these two observations actually probe a transient wind that evolves physically and geometrically throughout the black hole outburst?

We describe the observations and data analysis in Section 2. In Section 3, we present the *Chandra* spectra and use broadband X-ray spectra from the *Rossi X-ray Timing Explorer*'s (Jahoda et al. 1996) Proportional Counter Array (*RXTE* PCA) to study the ionizing continuum. We also build photoionization models to demonstrate how the wind responds to changes in the incident X-ray spectrum. In Section 4, we discuss the implications for the evolution of wind physics during the 2005 outburst.
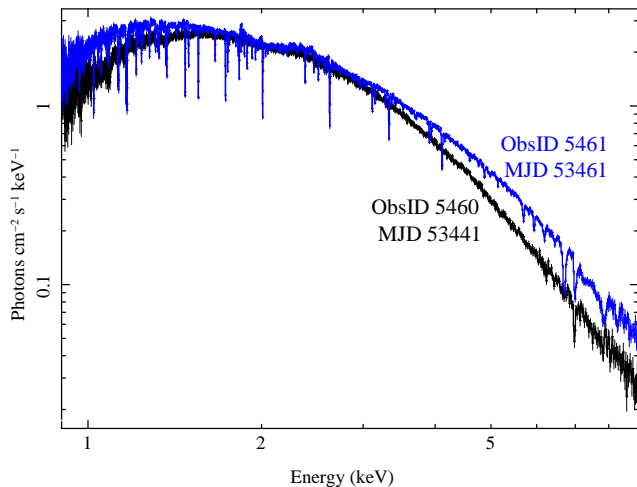
FIG. 1.— *Chandra* HETGS spectra of GRO J1655–40 during its 2005 outburst. Shown in black is the spectrum of the first observation, when the broadband X-ray continuum was hard and very few absorption lines were present; shown in blue is the spectrum of the second observation, which was executed 20 days later and recorded a rich series of lines from the accretion disk wind. In this paper, we address the physics driving these significant changes in the disk wind.

We conclude in Section 5.

2. OBSERVATIONS AND DATA REDUCTION

GRO J1655–40 was observed with the *Chandra* HETGS on 2005 March 12 (20:42:53 UT; ObsID 5460) and 2005 April 1 (12:40:41 UT; ObsID 5461) for 34.3 and 62.15 ks, respectively. The data were taken in Graded Continuous Clocking mode, which has a time resolution of 2.85 ms and is designed to limit both photon pileup and telemetry saturation.

We reduce and barycenter-correct the *Chandra* data with standard tools from the CIAO analysis suit, version 4.3. We use the order-sorting routine to remove the readout streak on the chip S4, since the dedicated tool (*destreak*) can also remove source counts when the count rate is high. After reprocessing, we extract High-Energy Grating (HEG) spectra and make grating response files.

During the *Chandra* observations, *RXTE* made pointed observations of GRO J1655–40 with good exposure times of 1.82 and 12.08 ks, respectively. In this paper, we analyze data from the PCA, which covers the 2–60 keV band, in order to explore the role of the photoionizing continuum in driving the evolution of the wind. For this spectral analysis, we extract Standard-2 129-channel spectra, and restrict our attention to the 3–45 keV spectrum from PCU2. We assume 0.6% systematic errors in each energy bin. All our spectral fitting is done in ISIS (Houck & Denicola 2000; Houck 2002). Following M08, we assume a neutral hydrogen column density $N_H = 7.4 \times 10^{21}$ cm^{-2} and a distance of 3.2 kpc (Orosz & Bailyn 1997).

3. X-RAY SPECTROSCOPY

The *Chandra* HEG spectra are shown in Figure 1, where it is abundantly clear that there are very significant differences between the absorber during the first (black) and second (blue) observations. In this section, we characterize the high-resolution and broadband spectra in an effort to determine whether photoionization alone can explain explain the differences in the lines. Our
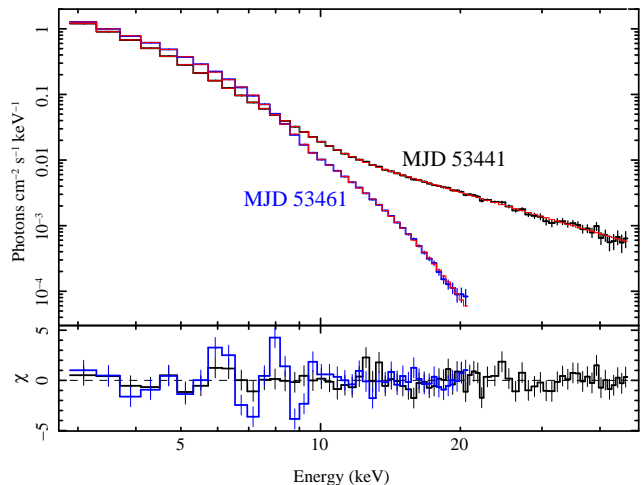

FIG. 2.— *RXTE* PCA spectra of GRO J1655–40 during its 2005 outburst. Shown in black is the spectrum of the first observation, when the broadband X-ray continuum was hard and very few absorption lines were present; shown in blue is the spectrum of the second observation, which occurred 20 days later and exhibits a significantly softer X-ray continuum. In Section 3 we argue that the changes in photoionizing flux are insufficient to explain the changes in the lines (Figure 1).

method is as follows: first we model the HEG/PCA spectra, then use XSTAR to calculate the expected atomic level populations for a gas slab illuminated by our observed ionizing continuum. Finally, we compare the predicted and observed absorption spectra. We focus on the first observation, which has not been studied in detail.

3.1. *Preliminary Modeling*

To start, we fit the HEG spectra phenomenologically with an absorbed polynomial spectrum and multiplicative Gaussian absorption lines (multiplicative absorption models are accurate even if the lines are moderately optically thick; Neilsen et al. 2012). The primary goal of this phenomenological modeling is not to catalog the lines or investigate their properties in detail (which has been done several times for the second observation, e.g. M08; K09), but to incorporate the ionized lines into models of the broadband X-ray spectrum as seen by *RXTE*. Thus we devote relatively little space in this section to a detailed discussion of the lines themselves.

However, a direct comparison of the Fe XXVI Lyα lines in the two observations is informative. In both spectra, we achieve tighter constraints on the parameters of these lines by fitting the Lyα and Lyβ lines simultaneously (i.e. with the same ion column density, velocity, and line width), since the optical depth in a line from any given ion is proportional to the line oscillator strength times the ion column density divided by the line width. Thus, even though Lyβ is not observed during observation 1, its absence places an upper limit on the column density of Fe XXVI. In the first observation, we find a column density $N_{\text{Fe xxvi}} = 6^{+2}_{-1} \times 10^{17}$ cm^{-2} and a blueshift of $v = -470 \pm 230$ km s^{-1} (the errors are 90% confidence limits). The line width is $\sigma = 13^{+8}_{-7}$ eV, and the equivalent width is $W_0 \approx 24$ eV. In the second observation, the Fe XXVI has a similar column density, $N_{\text{Fe xxvi}} = (7.6 \pm 0.9) \times 10^{17}$ cm^{-2}, but a higher velocity, width, and equivalent width ($v = -1350^{+170}_{-160}$ km s^{-1}, $\sigma = 21 \pm 4$ eV, and $W_0 \approx 31$ eV). In the second observation, at least 33 additional

strong features are present (in the 2.5-9 keV range) that are not visible in the first dataset.

In short, we see that the Fe XXVI column densities are similar, but all the other ion column densities increase dramatically from the first observation to the second, 20 days later. The simplest explanation for this fact is that the wind is more ionized during the earlier pointing. To test this hypothesis in more detail, we turn our attention to the broadband PCA spectra, which are shown in Figure 2. From this figure, the changes in the ionizing continua between the two observations are immediately apparent: during the first observation, there were many more photons capable of ionizing hydrogen- and helium-like iron (i.e. with $E \gtrsim 9$ keV). On the other hand, other elements have very small photoionization cross-sections for $E \gtrsim 9$ keV. So if the geometry or bulk properties of the wind were constant in time, we would expect there to be relatively little difference between the two observations in terms of absorption lines from ions other than iron. Since we observe highly-significant changes in lines other than iron, we can already conclude that excess ionizing luminosity alone is definitely not responsible for the absence of lines in the first observation.

Our best fit model for the broadband continuum in the first observation (`tbabs*(simpl ⊗ezdiskbb +egauss)*nmgauss*edges`) consists of an absorbed (`tbabs`; Wilms, Allen, & McCray 2000) hot disk (`ezdiskbb`; Zimmerman et al. 2005) convolved through a scattering kernel (`simpl`; Steiner et al. 2009), a Gaussian emission line at 6.4 keV, along with the Fe XXVI absorption line (`nmgauss`; Neilsen et al. 2012) detected in the HEG spectrum. `simpl` takes a seed spectrum and scatters a fraction f_{SC} of the source photons into a power law, approximating the high-temperature, low optical depth regime of Comptonization. Following Saito et al. (2006), we allow for possible ionized absorption edges at 7.7, 8.83, 9.28, and 10.76 keV, but none of these are detected at 90% confidence. Assuming a disk inclination of 67° (Orosz & Bailyn 1997) and a color correction factor of 1.7, the disk normalization $N = 390 \pm 20$ implies an inner disk radius $R_{in} = 29.1^{+0.7}_{-0.6}$ km, or roughly 2 gravitational radii, and the disk temperature is $T = 0.973 \pm 0.009$ keV. We find that $(5.6 \pm 0.3)\%$ of the disk photons are scattered into the power law, which has photon index $\Gamma = 2.11 \pm 0.04$. The implied unabsorbed luminosity (10^{-3}–10^3 keV) is $L = 6.4 \times 10^{37}$ ergs s^{-1}, roughly 7% of the Eddington limit. For the second observation, we include a `highecut` term to account for curvature in the spectrum; we can also replace `simpl⊗ezdiskbb` with `ezdiskbb+nthcomp` (Zdziarski et al. 1996; Życki et al. 1999). For our purposes here, only the luminosity of the second observation is relevant: $L \approx 5.7 \times 10^{37}$ ergs s^{-1}.

3.2. *Photoionization Modeling*

The immediate goal of our analysis is to determine why there are so few lines in the first observation. Are the changes in the luminosity and spectral shape enough to wipe out the lines? In Section 3.1 we argued that the answer is no, and that changes in the wind geometry or density are required. In this section, we make this argument quantitative with photoionization models.

The method itself is straightforward. We use XSTAR to calculate atomic data for an illuminated slab of gas. We define this slab of gas to match the properties of the wind seen in the *second* observation, as modeled by K09, and we illuminate it with the broadband X-ray spectrum of the *first* observation. In this way, we can test whether the same wind, ionized by a harder X-ray spectrum, should have been visible in the first dataset. For reference, we base our models on Model 6 of K09[2]: a density of $n = 10^{15}$ cm^{-3}, an equivalent column density $N_H = 10^{24}$ cm^{-2}, a 37% partial covering fraction, a blueshift of $v = 375$ km s^{-1}, and a turbulent line width of $v_{turb} = 200$ km s^{-1}. We increase the ionization parameter from $\xi = 10^4$ to $\xi = 10^{4.05}$ to account for the higher luminosity during the first observation. Finally, we use the elemental abundances reported in Figure 21 of K09.

We incorporate the resulting atomic data into new models of the HETGS observations using the analytic fit function `warmabs`. Using parameters equivalent to those measured by K09, but with an ionization balance appropriate for the first dataset, we find that there are a number of lines that would have been detected at high significance if the bulk properties of the wind were the same as those measured by K09 (see Figure 3). Three of the strongest features predicted by this test model but not observed in our data are Si XIV at 2.0, S XV at 2.6 keV, and Ar XVIII at 3.2 keV. To give an idea of how strong the features are, we note that without introducing any additional curvature into the spectrum (only lines), this test model increases χ^2 by over 1800 relative to a model with no wind at all. This result confirms our earlier conclusion: changes in the spectral shape and luminosity cannot be solely responsible for the absence of spectral lines in the first observation.

4. DISCUSSION

The results of our photoionization models in Section 3.2 are unequivocal: if the bulk properties of the wind were constant in time during the 2005 outburst of GRO J1655–40, a large number of strong lines should have been visible in the first dataset. A constant wind, simply over-ionized in the hard state, is ruled out. Furthermore, since the observations occur at orbital phases 0.5 and 0.0 (where the disk would be eclipsed at 0.75; Orosz & Bailyn 1997), orbital or companion star effects seem unlikely to be important. These results have broad implications for the role of winds in outburst (e.g. in quenching jets; Neilsen & Lee 2009). In this period of three weeks, as the source moved out of the hard, jet-producing state into a spectrally-soft state, the structure, density, or geometry of the accretion disk wind must have changed significantly. But what else can be said about the details of this evolving wind, given that so few lines are visible in the first dataset?

Most of what we know for certain comes from observation 2, which shows not only clear indicators of an MHD wind, but also compelling evidence for a second wind component: Kallman et al. (2009) found that while the typical blueshift of absorption lines in the spectrum is ~ 400 km s^{-1}, the strong lines of Fe XXVI and Ni XXVII are blueshifted by ~ 1300 km s^{-1}. See their Figure 15 for

---

[2] We compare our results to Kallman et al. (2009) rather than the original models of Miller et al. (2006a, 2008) because the newer models (at a higher density) provide a superior fit to the spectrum.
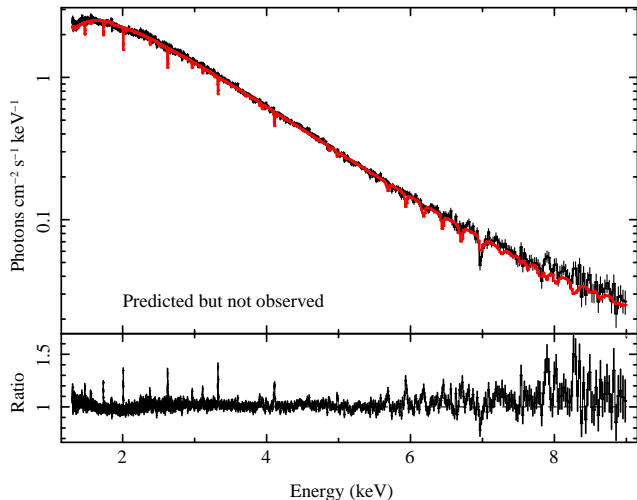
Fig. 3.— *Chandra* HETGS spectrum of the first observation of GRO J1655–40 (black) with model (red) based on the wind described by Kallman et al. (2009). If the wind were the same during both observations, a number of strong lines would have been seen during the first observation, despite its harder spectrum. That these lines are not observed indicates that the wind evolved significantly throughout the outburst.

TABLE 1
PHOTOIONIZATION MODELS OF GRO J1655–40

log n_w	log N_H	log ξ	log $n_{\Delta R}$	log $R_{\Delta R}$	log $n_{\Delta R/R}$	log $R_{\Delta R/R}$
11	$23.2^{+0.2}_{-0.2}$	$4.5^{+0.2}_{-0.1}$	14.2	9.5	13.9	9.7
12	$22.7^{+0.2}_{-0.2}$	$4.3^{+0.2}_{-0.1}$	13.7	9.9	12.8	10.4
13	$22.6^{+0.1}_{-0.2}$	$3.9^{+0.2}_{-0.1}$	13.6	10.2	12.0	11.0
14	$22.8^{+0.1}_{-0.2}$	$4.0^{+0.2}_{-0.1}$	13.8	10.0	12.5	10.7
15	$23.0^{+0.2}_{-0.2}$	$4.2^{+0.2}_{-0.1}$	14.0	9.8	13.2	10.2

NOTE. — n is the electron density input for XSTAR in cm^{-3}; N_H and ξ are the best-fit column density and ionization parameter for observation 1 in cm^{-2} and ergs cm s^{-1}; $n_{\Delta R}$ and $R_{\Delta R}$ are the density (cm^{-3}) and radius (cm) implied by the corresponding value of N_H if ΔR is fixed for the wind (Section 4.2.2); $n_{\Delta R/R}$ and $R_{\Delta R/R}$ are the density and radius implied by N_H if $\Delta R/R$ is fixed (Section 4.2.3).

a remarkable demonstration of this result, which they interpreted as indicative of a second, extremely highly ionized component. In fact, similar (although less extreme) differences in line dynamics have also been seen in other X-ray binaries. For example, studying an equally rich absorption line spectrum in GRS 1915+105, Ueda et al. (2009) found that while most lines were narrow and moderately blueshifted ($\sigma \sim 70$ km s^{-1}, $v \sim 150$ km s^{-1}), the Fe XXVI line was broader and faster ($\sigma \sim 200$ km s^{-1}, $v \sim 500$ km s^{-1}). Thus we are convinced that there is a two-component outflow in the second observation of GRO J1655–40. Since the magnetically-driven wind is a dense outflow at small radii, we suppose that the second component is a relatively low-density ($n \lesssim 10^{12}$ cm^{-3}) outflow at large radii ($R \gtrsim 10^{11}$ cm), i.e. as produced by thermal driving.

But how does this color our understanding of observation 1? Any explanation must hinge on the Fe XXVI line, which was present in both pointings. We focus on the bulk properties of the wind (i.e. density, location, and so on) in the hopes of determining the contributions of thermal and magnetic processes to the outflows in GRO J1655–40 (radiation pressure is ruled out for the same reason as in observation 2: it is ineffective at such high ionization parameters). So in short, it comes down to whether we believe the iron absorption line in the first spectrum should be associated with the slow, dense MHD component or the faster, more ionized thermal component in the second spectrum. Thus the interpretation of this line can be roughly separated into three scenarios, in which the wind in observation 1 is a purely thermal wind (Section 4.1), a magnetically-driven wind (already discussed in Section 3.2), or a hybrid thermal/MHD wind (Section 4.2).

While there is a very large body of literature on the theoretical aspects of the origin and properties of accretion disk winds (e.g. Begelman et al. 1983; Shields et al. 1986; Woods et al. 1996; Proga 2000; Proga & Kallman 2002; Luketic et al. 2010), there is relatively little information about which wind processes are expected to be most important at any given phase of a black hole outburst (cf. the unified model of disk-jet coupling in outburst; Fender et al. 2004). For example, are there links between the accretion state and the relative importance of radiatively-, thermally-, and magnetically-driven winds? Observations (Neilsen et al. 2012; Ponti et al. 2012) suggest that varying illumination and shadowing of the outer disk may be important in producing transient winds, but it is unclear how the density, launch radius, and geometry of these winds (MHD or thermal) should evolve over time. In the following subsections, we explore the implications of a variety of simple assumptions about the behavior of the wind in GRO J1655–40. By no means do these constitute an exhaustive list, but they should be representative of the possibilities.

4.1. *Case 1: A Thermal Wind in Observation 1*

Here, in light of the fact that Fe XXVI is present in both observations of GRO J1655–40, and may arise in a thermal wind in observation 2, we consider the possibility that this line also arises in a thermal wind during observation 1. In other words, we suppose that the thermal wind is persistent, while the MHD outflow is transient. This scenario is illustrated in Figure 4. Without decent estimates of the density or ionization parameter of the thermally-driven wind, it is very difficult to estimate its location. Thermally-driven winds can be launched anywhere outside 0.1 Compton radii ($R_C = 9.8 \times 10^{17} M_{BH} T_{IC}^{-1}$ cm; Begelman et al. 1983; Woods et al. 1996; Rahoui et al. 2010), where M_{BH} is the black hole mass in solar masses and the Compton temperature in Kelvins is given by:

$$T_{IC} = \frac{1}{4k_B} \frac{\int_0^\infty h\nu L_\nu d\nu}{\int_0^\infty L_\nu d\nu}, \qquad (2)$$

where h is Planck's constant, ν is the frequency, and L_ν is the monochromatic luminosity. For our PCA spectra of observations 1 and 2, we find $T_{IC} \sim 8.6 \times 10^7$ K and 8.4×10^6 K, respectively, which imply Compton radii $R_C \sim 8 \times 10^{10}$ cm and 8×10^{11} cm. The Compton temperature of the first observation is much higher because the spectrum is much harder; accordingly, Compton heating is more efficient and a thermal wind can arise at smaller radii.
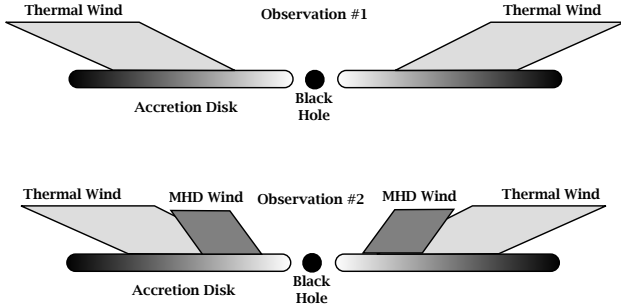
FIG. 4.— Cartoon of the scenario presented in Section 4.1, in which the wind in observation 1 is thermally-driven (top), while observation 2 (bottom) features a two-component wind, i.e. MHD and thermal. For the winds, darker shading implies higher density, and the different orientations of the two components reflects our uncertainty about the vertical component of the wind velocity. See text for details.
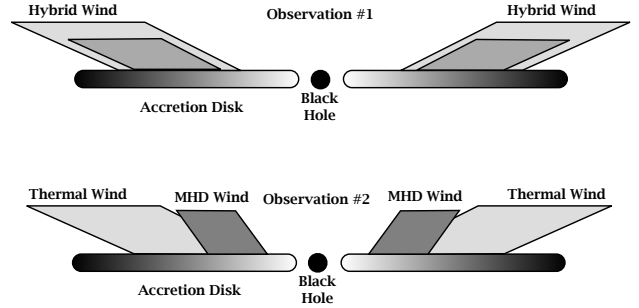

FIG. 5.— Cartoon of the scenario presented in Section 4.2, in which observation 1 (top) probes a hybrid wind driven by a combination of MHD and Compton heating. In this interpretation, the hybrid wind evolves over the course of weeks into two distinct outflows: a thermal wind at large radii and a MHD wind at small radii (bottom). See text for details, and see Figure 4 for notes about shading and orientation in these cartoons.

Importantly, in both cases, $0.1R_C$ is inside the disk, so that a Compton-heated wind is plausible at this radius.

The wind speed provides a different perspective. If we suppose that the wind speed is comparable to the local escape speed in the disk, then the thermal wind originates at 10^{12} cm and 10^{11} cm in the first and second observations, respectively. It is puzzling that the implied distance between the wind and the black hole in observation 1 is comparable to the binary separation. However, the wind velocity likely has a significant component perpendicular to the line of sight, so that the Doppler shift represents only a fraction of the true wind speed. But even if this is the case, the acceleration of the wind still requires some explanation. Why does the wind accelerate as the spectrum softens and the luminosity decreases? One possibility that has gained some ground recently (Neilsen et al. 2012; Ponti et al. 2012) is that during harder states, the geometrically-thick inner disk (e.g. Meier 2001) shadows some of the outer disk. This shadowing interpretation is potentially testable via optical/infrared measures of the irradiation of the companion star or outer disk (a paper on multiwavelength observations of this outburst is forthcoming). In this framework, as the scale height of the inner disk decreases during the state transition in GRO J1655–40, progressively smaller radii in the disk are irradiated, leading to a faster wind. A different irradiation geometry could also influence the direction of the wind velocity, e.g. driving it more into the line of sight in observation 2.

In summary, taken at face value, the estimates of R from the Compton radius and the escape velocity are not fully consistent. However, it may be possible to reconcile them by considering the vertical component of the wind velocity (which may be significant). Without a clear and unambiguous way to estimate the location or the density of this thermal wind, there is little more we can say about it. Nevertheless, we feel our estimates here are still merited, as there is compelling evidence for a two-component wind 20 days later (Kallman et al. 2009).

4.2. *Case 2: An Evolving Hybrid Wind*

On the other hand, given that observation 2 provides the only direct evidence for a magnetically-driven wind in an X-ray binary, it is also worth considering the possibility that both wind components (MHD and thermal)

are present in both observations of GRO J1655–40. In this scenario, illustrated in Figure 5, a precursor to the MHD wind makes a weak contribution to the Fe XXVI line in observation 1 (which is dominated by the thermal wind), but in the subsequent weeks evolves into the dense outflow discovered by M06. There is some circumstantial evidence to suggest that this scenario is plausible.

In particular, observations with *XMM-Newton* on 2005 March 18 and March 27 (i.e. six days after *Chandra* observation 1 and five days before *Chandra* observation 2, respectively) reveal the presence of an absorber with an ionization parameter that decreases rapidly over time (Díaz Trigo et al. 2007). Possible absorption lines were also detected with *Swift* (Brocksopp et al. 2006). It is very difficult to make a quantitative comparison of the winds seen by *Chandra* and *XMM-Newton* because the Doppler widths of the lines are so different: $\sigma \gtrsim 3000$ km s^{-1} in the *XMM-Newton* spectra and $\sigma \approx 600$ km s^{-1} in the *Chandra* observations. This difference may influence the apparent column density and ionization parameters. Nevertheless, Figure 5 of Díaz Trigo et al. (2007) indicates that between March 18 and March 27, the absorber began to resemble the forest of lines found by Miller et al. (2006a). In this context, it is also an interesting coincidence that the blueshift of the Fe XXVI line in observation 1 is the same as the blueshift of the slow MHD wind in observation 2.

Thus it is possible that a precursor to this MHD wind was present during the first *Chandra* observation. To explore this possibility, we expand on our XSTAR models from Section 3.2. In what follows, we consider a number of scenarios for what the properties of the precursor wind could have been during observation 1, or how they might have evolved during the outburst. To be clear, when we refer to a quantity as constant, we mean constant in time.

4.2.1. *Wind Density is Constant*

We begin with the assumption that the density of the MHD wind is constant during the outburst ($n = 10^{15}$ cm^{-3}), as in the XSTAR model shown in Figure 3. As discussed in Section 3.2, this model is dynamically identical to the wind in observation 2 (Kallman et al. 2009), but features an ionization balance appropriate for observation 1. In Section 3.2, we used this model in a simple test to show that the wind in observation 1 cannot

have the same column density and ionization parameter as it does in observation 2 (Figure 3). Here, we allow N_H and ξ to be free parameters and actually fit a `warmabs` model to the *Chandra* spectrum of observation 1. Using a 128×128 logarithmically-spaced grid covering $\xi = 10^3 - 10^5$ and $N_H = 10^{22} - 10^{24}$, we create a confidence map to search for the model that best fits this spectrum. The absence of lower-ionization lines and Fe XXVI Lyβ absorption provides upper limits on the column density of the model and lower limits on the ionization parameter, respectively. We allow the MHD precursor wind to contribute as much as possible to the Fe XXVI absorption line and assume the rest comes from the thermal wind. If the column density is too low, the predicted iron line will be too weak. Furthermore, because the column density is constrained from above, the ionization parameter cannot be arbitrarily high and still contribute to the line. Thus the Fe XXVI line provides lower limits on the column density and a upper bounds on the ionization parameter. For $n = 10^{15}$ cm^{-3}, we find an equivalent hydrogen column density $N_H = (9 \pm 4) \times 10^{22}$ cm^{-2} and an ionization parameter $\log \xi = 4.2^{+0.2}_{-0.1}$; the errors are 99% confidence limits for a single parameter. This result implies that the column density of the MHD wind increased by an order of magnitude between the first and second *Chandra* observations.

But the column density cannot be the only parameter that changes between these two observations, since

$$N_H = n \, \Delta R, \tag{3}$$

where ΔR is the (integrated) radial extent of the absorber. In general, in order for the column density to change, there must be variation in the gas density, the extent of the wind, or both. That is, in order to explain the differences in the *Chandra* lines, we require a significant change in at least one of these properties. In the model described in this section, the density is constant, which in turn implies from Equation 3 that ΔR must have been an order of magnitude smaller during observation 1 than it was 20 days later. Although this scenario is not impossible, it is unclear why the wind would have the same density but arise from a much smaller region of the disk or have a much smaller filling factor (i.e. why it would be so much clumpier). In other words, we cannot rule it out, but we are hesitant to accept a model in which the column density changes solely because of changes in ΔR.

4.2.2. ΔR is Constant

At the other extreme is the case where ΔR is constant, and the change in the wind column density between the two *Chandra* observations is due solely to a change in gas density. In this case, it is less straightforward to find the density of the wind during observation 1, because the ionization balance and resulting fits with `warmabs` are sensitive to the density, meaning that an iterative process is required. Ideally, to be fully self-consistent, we need the density n_w used to create the `warmabs` model to be the same as the density $n_{\Delta R}$ implied by Equation 3, i.e.:

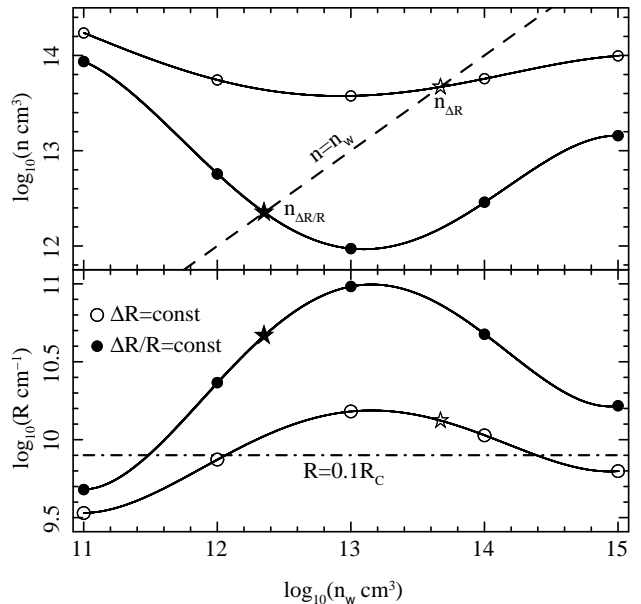$$n_w = n_{\Delta R} = \frac{N_{H,1}}{\Delta R} = n_2 \, \frac{N_{H,1}}{N_{H,2}}. \tag{4}$$

FIG. 6.— Densities (top) and radii (bottom) implied under various assumptions by our grid of `warmabs` models (at densities n_w) for the MHD precursor wind in *Chandra* observation 1. The open symbols correspond to the case where ΔR is constant during the outburst (Section 4.2.2), while the filled symbols correspond to the case where $\Delta R/R$ is constant (Section 4.2.3). The solid lines are polynomial interpolations of these data points; the dashed line in the top panel represents $n = n_w$. The intersection of an interpolation and $n = n_w$ is a self-consistent solution for the density of the wind in observation 1. These self-consistent solutions are shown as stars. In the bottom panel, $R = 0.1R_C$ is shown so that the implied radii may be compared to the smallest launch radius for the thermal component. See Section 4 for details.

Subscripts 1 and 2 refer to *Chandra* observations 1 and 2, respectively. To self-consistently determine the density for the scenario where ΔR is constant, we generate an additional set of `warmabs` models, which we fit to the *Chandra* spectrum of observation 1. Again, we use the same covering factor, turbulent line width, and blueshift as Kallman et al. (2009), but we build models with densities of $\log(n_w \text{ cm}^3) = 11, 12, 13, 14$, and 15. For each of these models, we perform the same grid search and confidence maps described in Section 4.2.1; the results for N_H and ξ are tabulated in Table 1. Typically, our best fit for any given model contributes only $\sim 3 - 4$ eV to the equivalent width of the Fe XXVI absorption line; the rest we attribute to the thermal component.

As in the preceding subsection, all of these models require that the column density of the MHD wind in observation 1 be more than an order of magnitude lower than it was in observation 2. Since we are assuming here that ΔR is constant, the density in observation 1 must be lower by the same factor. The implied densities $n_{\Delta R}$ are calculated from Equation 4, listed in Table 1, and plotted as open circles in the top panel of Figure 6; the bottom panel of this figure shows the corresponding radii from Equation 1. Interpolating over our (n_w, $n_{\Delta R}$) grid with a fourth-order polynomial, we solve for the density at which $n_{\Delta R} = n_w$. We find $n_{\Delta R} \approx 10^{13.7}$ cm^{-3} (indicated with an open star in Figure 6). At this density, Equation 4 is satisfied, so that the apparent change in the column density between the two *Chandra* observations is determined only by the change in density. Under these conditions, our constraints on the ionization parameter

of the precursor MHD wind in observation 1 imply a distance from the black hole of $R_{\Delta R} \approx 10^{10.1}$ cm. This is outside $0.1 R_{\rm C}$, i.e. it is consistent with the location of the thermal wind.

4.2.3. $\Delta R/R$ is Constant

Finally, we consider an intermediate scenario in which the changes in the column density are dictated by simultaneous changes in n and ΔR. If we suppose that $\Delta R/R$ is constant, i.e. the fractional extent of the wind does not change during the outburst, it is easy to show that the implied density $n_{\Delta R/R}$ is given by

$$ n_{\rm w} = n_{\Delta{\rm R/R}} = n_2 \left(\frac{\xi_1}{\xi_2}\right)\left(\frac{L_2}{L_1}\right)\left(\frac{N_{\rm H,1}}{N_{\rm H,2}}\right)^2 . \qquad (5) $$

Again, we are primarily interested in the self-consistent solution, where the column densities measured from the data with `warmabs` and the density input to XSTAR satisfy Equation 5, so that the fractional extent of the wind is preserved from one *Chandra* observation to the next. We employ the same iterative approach and `warmabs` models from Section 4.2.2; for each model, we calculate $n_{\Delta R/R}$ using our measurements of $N_{\rm H}$, ξ, and L (see Table 1 and the filled circles in Figure 6). The assumption that $\Delta R/R$ is constant leads to smaller densities and larger radii than the assumption that n or ΔR is constant. To find the self-consistent solution, we interpolate over our grid (filled circles in Figure 6) as before, and we find $n_{\Delta R/R} \approx 10^{12.4}$ cm^{-3} and $R_{\Delta R/R} \approx 10^{10.7}$ cm (filled stars in Figure 6). Once again, this location is also consistent with the location of the thermal wind.

To summarize the results of this section briefly, if we suppose that a magnetically-driven wind makes a contribution to the Fe XXVI absorption line in observation 1, then photoionization models require that this MHD wind have a lower column density than in observation 2. Considering self-consistent geometrical interpretations of this difference, we find it probable that wind has lower density and originates farther out in the first observation; in many cases its location is consistent with that of the thermally-driven wind. Thus, in this scenario, the wind found in the first observation may actually be a hybrid MHD/thermal wind.

5. SUMMARY AND CONCLUSIONS

In this paper, we have explored the puzzling variability of the accretion disk wind of the black hole GRO J1655–40, as seen by *Chandra* during the 2005 outburst. The first *Chandra* HETGS observation, taken in March of that year as the source was beginning a transition out of the hard state, revealed a single Fe XXVI absorption line at 7 keV; in a much softer state twenty days later, *Chandra* saw a forest of hundreds of lines (Kallman et al. 2009), indicative of one of the densest, highest-column winds observed in an X-ray binary to date (so dense and so highly ionized that magnetic processes must have been the primary launching mechanism; Miller et al. 2006a, 2008).

But how are we to interpret the relatively sudden appearance of so many lines? Is it possible that state-dependent changes in the ionizing spectrum dominate changes in the optical depth in the wind, or is a strongly variable outflow required to account for the variable lines? In Section 3.2, we showed that the wind could not possibly have been the same in both *Chandra* observations, or else both spectra would have shown similar numbers of strong absorption lines. In fact, not only is the broadband spectrum in observation 1 incapable of over-ionizing the wind discovered by M06, it should actually be *better* at driving a thermal wind off the disk!

Armed with the certainty that the wind must have changed during the outburst, we considered in Section 4 some of the ways that it might have evolved from one *Chandra* observation to the next. This was not meant to be an exhaustive study of every conceivable variant of the geometry of the wind, but a focused exploration of some of the cleanest explanations. In Section 4.1, we considered the possibility that there might be two physically-distinct outflows in GRO J1655–40 (see Kallman et al. 2009 for dynamical evidence for this conclusion), one persistent Compton-heated wind and one transient MHD wind. In Section 4.2, we considered several alternate scenarios in which both the thermal component and the MHD component were present in both observations; we modeled the MHD component with a grid of XSTAR models to constrain its properties. In these scenarios, the absence of so many lines during the first *Chandra* observation indicates a significantly smaller column density for the precursor MHD wind, which could be due to changes in its radial extent, thickness, or filling factor, its density, or both. In the latter two cases, the location of the MHD component is consistent with the location of the thermal component (implied by the measured ionization parameter and Compton temperature, respectively).

Although there is no compelling empirical evidence highlighting any of these scenarios as preferable, there is tantalizing evidence from contemporaneous *XMM-Newton* observations (Díaz Trigo et al. 2007) that the single-line wind detected in the first *Chandra* observation might evolve smoothly into the rich, dense outflow discovered by Miller et al. (2006a), with a second, more ionized and faster component mentioned by Kallman et al. (2009). Following this line of reasoning, we suggest that the first *Chandra* observation might be probing a hybrid MHD/thermal wind from the outer disk that evolves over the next three weeks into two distinct flows with very different properties. Future theoretical work on the expected behavior of disk winds in outburst may shed more light on these results, and whether thermal wind models can actually produce the observed lines (see Luketic et al. 2010). For the moment, it is remarkable that such insights, even if tentative, can be gleaned from a spectrum with only one line. But we have the benefit of a great deal of context from other observations during the outburst, as well as high-quality spectra from *RXTE*.

Regardless of the precise physical explanation, it is abundantly clear that the differences between the two *Chandra* spectra cannot be explained by differences in the number of ionizing photons. Instead, the changes in the wind are very likely linked in a fundamental way to the state of the accretion disk (see also Lee et al. 2002; Schulz & Brandt 2002; Miller et al. 2006b, 2008; Neilsen & Lee 2009; Blum et al. 2010; Neilsen et al. 2011, 2012). It would be particularly interesting if the changes in the magnetically-driven wind could be tied to changes in the magnetic field configu-

ration in different states, but different accretion rates, radiative efficiencies, and scale heights in the inner accretion disk (e.g. Neilsen et al. 2012; Ponti et al. 2012) may also be important. In a forthcoming paper, we will perform a comprehensive study of the radio, infrared, and X-ray emission in order to explore the relationship between the accretion state and the wind in much more detail.

REFERENCES

Begelman, M. C., McKee, C. F., & Shields, G. A. 1983, ApJ, 271, 70
Blum, J. L., Miller, J. M., Cackett, E., et al. 2010, ApJ, 713, 1244
Brandt, W. N. & Schulz, N. S. 2000, ApJ, 544, L123
Brocksopp, C., McGowan, K. E., Krimm, H., et al. 2006, MNRAS, 365, 1203
Canizares, C. R., Davis, J. E., Dewey, D., et al. 2005, PASP, 117, 1144
Díaz Trigo, M., Parmar, A. N., Miller, J., Kuulkers, E., & Caballero-García, M. D. 2007, A&A, 462, 657
Ebisawa, K. 1997, in X-Ray Imaging and Spectroscopy of Cosmic Hot Plasmas, ed. F. Makino & K. Mitsuda, 427-+
Fender, R. P., Belloni, T. M., & Gallo, E. 2004, MNRAS, 355, 1105
Houck, J. C. 2002, in High Resolution X-ray Spectroscopy with XMM-Newton and Chandra, ed. G. Branduardi-Raymont
Houck, J. C. & Denicola, L. A. 2000, in Astronomical Society of the Pacific Conference Series, Vol. 216, Astronomical Data Analysis Software and Systems IX, ed. N. Manset, C. Veillet, & D. Crabtree, 591-+
Jahoda, K., Swank, J. H., Giles, A. B., et al. 1996, in Society of Photo-Optical Instrumentation Engineers (SPIE) Conference Series, Vol. 2808, Society of Photo-Optical Instrumentation Engineers (SPIE) Conference Series, ed. O. H. Siegmund & M. A. Gummin, 59–70
Kallman, T. R., Bautista, M. A., Goriely, S., et al. 2009, ApJ, 701, 865
King, A. L., Miller, J. M., Raymond, J., et al. 2012, ApJ, in press
Kotani, T., Ebisawa, K., Dotani, T., et al. 2000a, ApJ, 539, 413
Kotani, T., Kawai, N., Matsuoka, M., et al. 1997, in American Institute of Physics Conference Series, Vol. 410, Proceedings of the Fourth Compton Symposium, ed. C. D. Dermer, M. S. Strickman, & J. D. Kurfess, 922–926
Kotani, T., Ebisawa, K., Inoue, H., et al. 2000b, Advances in Space Research, 25, 445
Lee, J. C., Reynolds, C. S., Remillard, R., et al. 2002, ApJ, 567, 1102
Luketic, S., Proga, D., Kallman, T. R., Raymond, J. C., & Miller, J. M. 2010, ApJ, 719, 515
Meier, D. L. 2001, ApJ, 548, L9
Miller, J. M., Raymond, J., Fabian, A. C., et al. 2004, ApJ, 601, 450

Miller, J. M., Raymond, J., Fabian, A., et al. 2006a, Nature, 441, 953
Miller, J. M., Raymond, J., Homan, J., et al. 2006b, ApJ, 646, 394
Miller, J. M., Raymond, J., Reynolds, C. S., et al. 2008, ApJ, 680, 1359
Miller, J. M., Maitra, D., Cackett, E. M., Bhattacharyya, S., & Strohmayer, T. E. 2011, ApJ, 731, L7+
Neilsen, J. & Lee, J. C. 2009, Nature, 458, 481
Neilsen, J., Remillard, R. A., & Lee, J. C. 2011, ApJ, 737, 69
Neilsen, J., Petschek, A. J., & Lee, J. C. 2012, MNRAS, 2287
Orosz, J. A. & Bailyn, C. D. 1997, ApJ, 477, 876
Ponti, G., Fender, R., Begelman, M., et al. 2012, MNRAS, in press
Proga, D. 2000, ApJ, 538, 684
Proga, D. & Kallman, T. R. 2002, ApJ, 565, 455
Rahoui, F., Chaty, S., Rodriguez, J., et al. 2010, ApJ, 715, 1191
Reynolds, M. T. & Miller, J. M. 2010, ApJ, 723, 1799
Saito, K., Yamaoka, K., Fukuyama, M., et al. 2006, in VI Microquasar Workshop: Microquasars and Beyond
Schulz, N. S. & Brandt, W. N. 2002, ApJ, 572, 971
Shields, G. A., McKee, C. F., Lin, D. N. C., & Begelman, M. C. 1986, ApJ, 306, 90
Steiner, J. F., McClintock, J. E., Remillard, R. A., Narayan, R., & Gou, L. 2009, ApJ, 701, L83
Tarter, C. B., Tucker, W. H., & Salpeter, E. E. 1969, ApJ, 156, 943
Ueda, Y., Murakami, H., Yamaoka, K., Dotani, T., & Ebisawa, K. 2004, ApJ, 609, 325
Ueda, Y., Yamaoka, K., & Remillard, R. 2009, ApJ, 695, 888
Wilms, J., Allen, A., & McCray, R. 2000, ApJ, 542, 914
Woods, D. T., Klein, R. I., Castor, J. I., McKee, C. F., & Bell, J. B. 1996, ApJ, 461, 767
Zdziarski, A. A., Johnson, W. N., & Magdziarz, P. 1996, MNRAS, 283, 193
Zimmerman, E. R., Narayan, R., McClintock, J. E., & Miller, J. M. 2005, ApJ, 618, 832
Życki, P. T., Done, C., & Smith, D. A. 1999, MNRAS, 309, 561